AAPS PharmSciTech, Vol. 15, No. 1, February 2014 (© 2013)
DOI: 10.1208/s12249-013-0041-3

Research Article

Novel Self-assembly Endows Human Serum Albumin Nanoparticles with an Enhanced Antitumor Efficacy

Dawei Ding,[1] Xiaolei Tang,[1] Xiaoli Cao,[1] Jinhui Wu,[1,3] Ahu Yuan,[1] Qian Qiao,[1] Jing Pan,[2] and Yiqiao Hu[1,3]

Received 23 April 2013; accepted 8 October 2013; published online 28 November 2013

Abstract. Protein-based nanomedicine plays an important role in tumor chemotherapy due to their merits in bioavailability, biocompatibility, biodegradability, and low toxicity. In this study, we developed a novel method of preparing human serum albumin (HSA) nanoparticles for targeted delivery of paclitaxel (PTX) to tumors. HSA-PTX nanoparticles (NPs-PTX) were fabricated via unfolding of HSA in appropriate solution to expose more hydrophobic domains and consequent self-assembling into nanoparticles with added PTX. Via this self-assembly method, a desirable particle size (around 120 nm), a high drug loading (>20%), and a high encapsulation efficiency (near 100%) were obtained. PTX dispersed as an amorphous state in NPs-PTX and the secondary structures of HSA were maintained. In a cytotoxicity study, NPs-PTX displayed an enhanced cytotoxicity in MCF-7 and A549 cells. Confocal microscopy and flow cytometry revealed that the uptake of NPs-PTX was mediated by secreted protein acidic and rich in cysteine and "caveolar" transport. In H22 tumor-bearing mice, NPs-PTX displayed an increasing and everlasting tumor distribution, leading to slower tumor growth and longer mice survival than PTX. Therefore, this novel self-assembly method offers a much easier method to prepare PTX nanoparticles, provides better antitumor efficacy *in vitro* and *in vivo*, and more importantly, sets up a delivery platform for other hydrophobic drugs to improve their effectiveness in cancer therapy.

KEY WORDS: human serum albumin; nanoparticles; paclitaxel; self-assembly; targeted drug delivery.

INTRODUCTION

Nowadays, it is of considerable interest and necessity to encapsulate clinically authorized drugs into nanoscale delivery vehicles such as liposomes, dendrimers, micelles, and polymer–drug conjugates for cancer chemotherapy (1,2). Nanocarriers have been shown to accumulate within solid tumors due to the enhanced permeability and retention (EPR) effect arising from the abnormalities in blood and lymphatic vasculatures in tumor (3–6). However, only a few of them, such as Doxil® (pegylated doxorubicin liposome) and Myocet® (doxorubicin liposome), were approved by the Food and Drug Administration (FDA) for clinical use (1). A majority of nanocarriers failed in preclinical research or were terminated in clinical trials (7–10), since they were not able to simultaneously control their stability, biocompatibility, biodegradability, and toxicity (1,11–13). Thus, greater efforts are still needed to achieve a more ideal drug delivery system (easily fabricated, stable, biodegradable, biocompatible, and nontoxic) (2,4,14,15).

Current researches are focusing upon protein-based nanocarriers, which employ endogenous protein such as albumin and transferrin as a template to encapsulate different drugs into particles (14). Proteins are nontoxic and able to degrade into amino acids which could be utilized by peripheral tissue (16). Besides the traditional features such as passive targeting and extended half-life (8,17), active targeting delivery is also integrated within protein-based nanoparticles. For example, albumin was reported to show high affinity with gp60 and secreted protein acidic and rich in cysteine (SPARC) that are overexpressed on tumor cell surfaces and, thereby, could be used for tumor targeting (18,19).

Many strategies have been reported for fabricating protein-based nanoparticles, including emulsification, self-assembly, desolvation, and thermal gelation (16). Among them, emulsification had been extensively evaluated (16), and an outstanding case, Abraxane®, which was an albumin-based nanoparticle for the delivery of paclitaxel (PTX), was successfully approved by the FDA in 2005 for the treatment of breast cancer (18,20). The preparation method highly relied on subjecting a mixture of protein and drug to a high-pressure homogenizer to achieve a nanoscale emulsion. However, the high pressure and complicated procedure may not be suitable

Dawei Ding and Xiaolei Tang contributed equally to this work.

Electronic supplementary material The online version of this article (doi:10.1208/s12249-013-0041-3) contains supplementary material, which is available to authorized users.

[1] State Key Laboratory of Pharmaceutical Biotechnology, Nanjing University, Nanjing 210093, People's Republic China.
[2] Department of Pharmaceutics, China Pharmaceutical University, Nanjing 210009, People's Republic China.
[3] To whom correspondence should be addressed. (e-mail: wuj@nju.edu.cn; huyiqiao@nju.edu.cn)

for some temperature-sensitive agents and proteins (16). In addition, the organic solvent (dichloromethane) employed in preparation is also an issue since a little amount of residual is toxic to the liver, kidney, lungs, and neural system (21).

Apart from emulsification, extensive attention has been paid to self-assembling nanoparticles. This self-assembly strategy commonly employs covalent conjugations, which could improve the hydrophobicity of proteins and drive them to self-assemble into nanoparticles (17,22). For instance, albumin has been conjugated with doxorubicin (DOX) for self-assembling into nanoparticles (22–24). Recombinant elastin-like polypeptides were also reported to attach to DOX and self-assemble into nanoparticles (2,17,25). These conjugations were achieved by the covalently attached maleimide group of DOX to cysteine residues. Nonetheless, there are still many limitations for this covalence-based self-assembly. First, complicated chemical synthesis was commonly employed in fabricating conjugations (2,22). Second, the toxicity of residual chemical cross-linking agents in conjugations remains a major problem (16,26).

To overcome the previously mentioned limitations, we herein report a novel self-assembling human serum albumin (HSA) nanoparticle for targeted delivery of PTX. In this study, HSA was unfolded to expose more hydrophobic domains and self-assembled into nanoparticles with PTX (27). This strategy efficiently eliminates the defects in complicated synthesis as well as the toxicity of residual conjugating agents and organic solvents in Abraxane® and other formulations. The physicochemical characteristics, *in vitro* cellular uptake, and real-time *in vivo* biodistribution of HSA-PTX nanoparticles (NPs-PTX) were investigated, while their *in vitro* and *in vivo* antitumor efficacies were evaluated and compared with Abraxane®.

MATERIALS AND METHODS

Materials

PTX was purchased from Zelang Medical Technology Co., Ltd. (Nanjing, China). HSA was bought from CSL Behring (Marburg, Germany). Abraxane® was purchased from Jingwei Pharmacy Co., Ltd. (Nanjing, China). β-Mercaptoethanol (β-ME) and methyl-β-cyclodextrin (β-CD) were bought from SunshineBio Co., Ltd. (Nanjing, China). Coumarin-6 (Cou-6) and NIR-775 were obtained from Sigma-Aldrich (St. Louis, MO, USA). Other organic solutions were purchased from Sinopharm Chemical Reagent Co., Ltd. (Beijing, China). Human breast cancer cell line MCF-7, human lung cancer cell line A549, and murine hepatic carcinoma cell line H22 were cultured by the State Key Laboratory of Pharmaceutical Biotechnology (Nanjing, China). Male ICR mice (6–8 weeks of age and weighting 18–22 g) were purchased from Qinglongshan Experimental Animal Center (Nanjing, China). ICR strain mice are from the Swiss Hauschka mice group and developed by the American Institute for Cancer Research (Washington, DC, USA). All studies were carried out in accordance with the Institutional Animal Care Committee at Nanjing University.

Preparation of NPs-PTX

HSA was dissolved in water (2 mg/mL) and mixed with β-ME. Then, PTX (10 mg/mL, dissolved in ethanol) was slowly added into the denatured protein solution according to various drug/protein ratios. The color of the solution changed into slight blue and PTX-loaded HSA nanoparticles were formed. After that, the mixed solution was dialyzed against water for 24 h to remove β-ME and then freeze-dried for further use.

Characterization of NPs-PTX

Size, Zeta Potential, and Morphology of NPs-PTX

The mean diameter and size distribution of NPs-PTX were determined by dynamic light scattering (DLS) with a particle size analyzer (90Plus, Brookhaven Instruments Corporation, Holtsville, NY, USA). The zeta potential of nanoparticles was measured with a zeta potential analyzer (ZetaPlus, Brookhaven Instruments Corporation, Holtsville, NY, USA). Each sample was diluted to a protein concentration of 0.2% (*w*/*v*) with water before the measurements of triplicate samples.

The morphology of NPs-PTX was investigated by transmission electron microscopy (TEM, JEM-2100, JEOL, Tokyo, Japan) and scanning electron microscopy (SEM, S-3400N, HITACHI, Tokyo, Japan). In TEM examination, NPs-PTX were dissolved in water and dried overnight on a copper grid before observation. For SEM examination, NPs-PTX were dispersed in 0.65% glycerol, spread onto a cover slide, immobilized in 2% formaldehyde, and dehydrated in a graded series of ethanol–water solutions. Finally, it was coated with a layer of platinum before being subjected to SEM.

HPLC Analysis of PTX, Drug Loading Content, and Encapsulation Efficiency

NPs-PTX with different drug/protein ratios were prepared and lyophilized according to the method in the "Preparation of NPs-PTX" section. The reconstituted nanoparticles were diluted in tenfold volume of acetonitrile (high-performance liquid chromatography [HPLC] grade, Merck, Whitehouse Station, NJ, USA), and vortexed for 1 min, centrifuged at 16,000 rpm for 5 min, and then the supernatant was injected into the HPLC system with a HC-C18 column (250×4.6 mm, 5 μm, C18, Agilent, Santa Clara, CA, USA). The mobile phase consisted of 40/60 water/acetonitrile (HPLC grade, Merck, Whitehouse Station, NJ, USA). The flow rate was set as 1.0 mL/min, while the UV detection wavelength was 227 nm. The drug loading content and encapsulation efficiency were calculated by Eqs. 1 and 2, respectively:

$$\text{Drug loading content } \% = \frac{\text{Weight of the drug in nanoparticles}}{\text{Weight of the nanoparticles}} \times 100\% \quad (1)$$

$$\text{Encapsulation efficiency } \% = \frac{\text{Weight of the drug in nanopaticles}}{\text{Weight of the feeding drug}} \times 100\% \quad (2)$$

In Vitro Stability of NPs-PTX

We employed bovine serum and isotonic solutions including 0.9% NaCl and 5% glucose to evaluate the stability of NPs-PTX by detecting their mean diameter at 37°C and room temperature, respectively. Briefly, nanoparticles were reconstituted in 0.9% NaCl and 5% glucose at 25°C as well as in bovine serum at 37°C with a protein concentration of 5 mg/mL. In the following 1, 3, 6, 12, 18, 24, and 36 h, mean particle diameters were investigated by DLS.

Detection of Status of PTX and HSA in NPs-PTX

X-ray powder diffraction (XRD) was utilized to detect the status of PTX. There were five samples in this examination, including PTX crystal, HSA powder, and the physical mixtures of PTX and HSA (1:9, *w*/*w*) and NPs-PTX (1:9 PTX/HSA, *w*/*w*) and Abraxane®. After being fully mulled, they were examined under an X-ray diffractometer (XTRA/3KW, ARL, Ecublens, Switzerland), while the wavelength was 1.5418 Å and the incidence angle 2θ was from 3° to 45°.

Also, we employed the circular dichroism spectrum (CD) to investigate the change in secondary structures of HSA before and after the fabrication of NPs-PTX and compare with Abraxane®. Briefly, Abraxane®, HSA, and NPs-PTX were dissolved in water with the concentration of protein at 10 μg/mL and subjected to a CD spectropolarimeter (J-810, Jasco, Tokyo, Japan), while the ellipticity was measured at the wavelength from 190 to 250 nm. Then, the respective proportions of different secondary structures, such as α helix, β sheet, and random coil, were calculated according to the method of Yang *et al.* (28,29).

In Vitro Cytotoxicity of NPs-PTX

The *in vitro* cytotoxicity of NPs-PTX on human breast cancer cell line MCF-7 and human lung cancer cell line A549 was evaluated by the MTT assay (30). Briefly, 2,000 cells/well were seeded in 96-well plates (CoStar, Washington, DC, USA) and then incubated for 12 h at 37°C for cell adhesion. Then, 10 μL of a serial concentration of PTX (dissolved in Cremophor EL/ethanol 1:1 *v*/*v* and diluted with phosphate-buffered saline [PBS]), NPs-PTX, and Abraxane® with equivalent PTX concentrations were added to each well, with 10 μL PBS in medium as control, and incubated for another 48 h. In the following, 30 μL of MTT indicator dye (4 mg/mL in PBS, pH 7.4) was added into each well, and cells were incubated for another 4 h. Then, the medium was removed and 150 μL DMSO was added in each well to dissolve the crystals of dye. Finally, the solution was measured at a 490-nm test wavelength and a 690-nm reference wavelength on a microplate reader (Safire, Tecan, Männedorf, Switzerland). Value obtained was expressed as a percentage of the control cells. Based on the results, the IC_{50} values were calculated.

Cellular Uptake of NPs-PTX

To detect the MCF-7 cellular uptake of NPs-PTX, Cou-6 was employed as a fluorescent marker (31,32). Briefly, PTX and Cou-6 (100:1, *w*/*w*) were added simultaneously to form NPs-PTX-Cou-6 during the preparation of nanoparticles. MCF-7 cells were seeded into six-well plates (CoStar, Washington, DC, USA) and incubated for 12 h at 37°C for cell adhesion and incubated for another 4 h with added NPs-PTX-Cou-6. In the following, cells were rinsed with cold PBS to stop the uptake, fixed with 4% paraformaldehyde for 20 min, and stained by 4′,6-diamidino-2-phenylindole (DAPI) for 15 min before being observed under the confocal laser scanning microscope (CLSM, FV1000, Olympus, Tokyo, Japan). To investigate whether nanoparticles interacted with tumor cells via HSA receptors overexpressed on tumor cells (18,33), MCF-7 cells cultured in serum-free media were preincubated with low (0.4 mg/mL) and high (4 mg/mL) concentrations of free HSA for 2 h before they were exposed to NPs-PTX-Cou-6. On the other aspect, MCF-7 cells were preincubated with low (1 mM) and high (2 mM) concentrations of β-CD for 1 h before they were exposed to NPs-PTX-Cou-6.

Moreover, flow cytometry (FCM) was utilized to quantitatively confirm if NPs-PTX was internalized into tumor cells. MCF-7 cells were preincubated with PBS, low (0.4 mg/mL) and high (4 mg/mL) concentrations of free HSA for 2 h, as well as PBS, low (1 mM) and high (2 mM) concentrations of β-CD for 1 h, respectively. Afterwards, they were exposed to NPs-PTX-Cou-6 for 4 h incubation. Cells with no treatment were set as the control. All mediums were removed and trypsin was added to digest the cells, after which they were centrifuged and rinsed with cold PBS. Finally, FCM (FACScalibur, BD, San Jose, CA, USA) was employed to detect the fluorescence intensity of cells.

Real-Time Biodistribution of NPs-PTX

The real-time *in vivo* biodistribution of NPs-PTX was evaluated by near infrared fluorescent system (NIRF). NIR-775 was utilized to label NPs-PTX. Briefly, in the preparation process, NIR-775 was dissolved in the PTX solution and was co-assembled into nanoparticles (NPs-PTX-NIR-775). Meanwhile, the H22 tumor model was developed by subcutaneously inoculating H22 cells to the ICR mice at the right axilla. In the following, free NIR-775 and NPs-PTX-NIR-775 with equivalent NIR-775 concentration were injected into tumor-bearing mice via the tail vein. At different time intervals (0.5, 1, 3, 6, 10, 24, 48, and 72 h) after intravenous (i.v.) administration, the biodistribution was imaged utilizing the IVIS® Lumina System (Xenogen, Alameda, CA, USA) with an excitation wavelength at 745 nm. The NIRF images at 800 nm were collected and exposure time was set as 1 s.

In Vivo Antitumor Efficacy of NPs-PTX

In the H22 tumor model, tumor was measured by a vernier calipers each day and its volume (V) was calculated as $V=d^2\times D/2$, where d and D are the shortest and the longest diameters of the tumor in millimeters, respectively. Treatments were started when tumor reached a volume of about 100 mm^3 (designated as day 1). Mice were randomly divided into three groups (n=4–5). On days 1 and 3, mice were administered intravenously with PTX, NPs-PTX, and Abraxane®, respectively. PTX was given at its MTDs (13.4 mg PTX/kg) (19), while NPs-PTX and Abraxane® were administered at the PTX doses of 30 mg/kg. The control group was given saline only. Afterwards, the mean tumor volumes were

measured every day and the survival rate of animals was also recorded.

Statistical Analysis

Results were presented as the mean±standard deviation (SD) if there is no special explanation. Data were analyzed by one-way analysis of variance. When overall statistical significance was achieved ($P<0.05$), Dunnett's multiple range test was used to compare each of the doses to the vehicle control. Probability values <0.05 were considered to be significant.

RESULTS AND DISCUSSION

Preparation of NPs-PTX

In this study, we pioneered a novel self-assembly method via protein unfolding to encapsulate antitumor drugs into nanoparticles. This method avoided the complexity of fabrication procedure and the toxicity of residual chemical agents encountered in the fabrication of Abraxane®, as well as provided a mild preparation condition for drugs and proteins. HSA was a global molecule with hydrophobic domains in the inner core and hydrophilic domains in the surface layer (34,35). When unfolded in β-ME, disulfide bonds were reduced. Thus, hydrophobic domains were exposed and consequently interacted with hydrophobic PTX, which finally self-assembled into nanoparticles. This process was demonstrated by the color change of the solution from achromatism to slight blue (Supplementary Fig. 1).

Characterization of NPs-PTX

Size, Zeta Potential, Morphology, and PTX Analysis of NPs-PTX

The DLS experiment indicated the formation of NPs-PTX with a hydrodynamic diameter around 120 nm and a relatively narrow size distribution (polydispersity<0.1) (Fig. 1a). This size is a bit smaller than that of Abraxane®, making nanoparticles a bit easier to accumulate in tumors due to the EPR effect (11). The representative TEM and SEM of NPs-PTX were shown, respectively. In the TEM and SEM images, NPs-PTX was spherical and smooth (Fig. 1b, c).

To evaluate the effect of drug/protein ratio on particle characteristics, a series of nanoparticles with ratios from 0% to 30% (*w*/*w*) were prepared (Table I). The mean particle size of HSA (no drug) was around 15 nm and it was increased to about 130 nm when the ratio went up to 5%. From 5% to 20%, the mean diameter was not significantly changed, while it exceeded 160 nm when the ratio was increased from 20% to 30%. We speculated that this step-increasing profile of particle size might be due to the fact that there were still large amounts of single HSA molecules when adding only 5% PTX. They could be involved in forming more nanoparticles when the ratio was within 20%, thereby no increase in mean particle size was observed. When the ratio went beyond 20%, no single HSA was available; hence, PTX had to interact with existing nanoparticles, thus increasing the mean particle size. The drug loading capacity was slowly and linearly increased with the increase of PTX and could be encouragingly high up to over 20% when the drug/protein ratio approached 30%. The encapsulation efficiency also varied with different drug/protein ratios. It was increased to near 100% when the ratio reached 15%, which meant nearly all drugs were encapsulated into the nanoparticles, but gradually decreased when the ratio surpassed 15%. This might result from the fact that the interaction between protein and drug was attenuated upon existing binding of PTX, causing that nanoparticles could not encapsulate more PTX. In all NPs-PTX with various drug/protein ratios, their zeta potential stayed stable at about −20 to −30 mV. This might result from the fact that the solution's pH was higher than the isoelectric point of HSA, thus giving negative charges to proteins. The negative charges guaranteed the stability of nanoparticles in aqueous surroundings. In this study, NPs-PTX with drug/protein ratio at 15% was utilized in the following experiments if there is no special explanation.

In Vitro Stability of NPs-PTX

To evaluate the stability of NPs-PTX, the changes of particle size were recorded in different solutions. In 0.9% NaCl and 5% glucose, mean particle size of NPs-PTX remained constant for 36 h at 25°C, while that in bovine serum remained steady for 24 h at 37°C and rose a little thereafter (Fig. 2). This suggested that NPs-PTX was more stable. Stability was one of the most crucial factors for the clinical use of drug formulation since the drug might slowly escape from nanoparticles and formed secondary aggregates, thereby possibly leading to the blood vessel occlusion and making them more susceptible to clearance by the mononuclear phagocytic system cells (36). The high stability also ensured that NPs-PTX could have a long circulation time *in vivo*, an

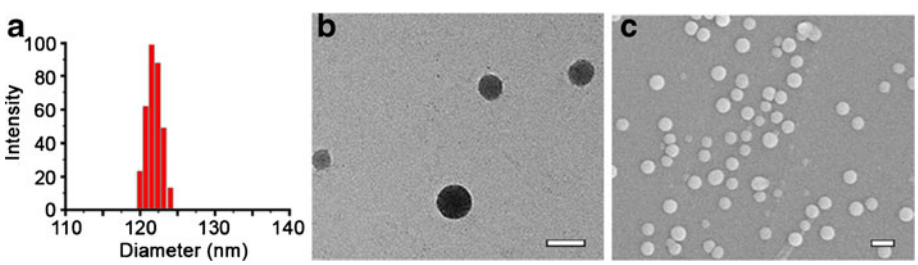

Fig. 1. Characterization of NPs-PTX. **a** Particle size and size distribution of NPs-PTX determined by DLS. **b** TEM image of NPs-PTX. The scale bar stands for 100 nm. **c** SEM image of NPs-PTX. The scale bar stands for 400 nm

Table I. Characteristics of NPs-PTX with Varying Drug/Protein Ratios (n=3)

PTX/HSA ratios (w/w)	Diameter[a] (nm)/PI	Zeta potential (mV)	DL (%)	EE (%)
0	16.23±1.47/0.031	−4.21±4.04	N.A.	N.A.
5%	131.47±6.66/0.050	−28.27±6.78	3.45±0.04	74.5±0.9
10%	123.86±8.23/0.083	−32.27±11.84	7.77±0.01	84.6±0.1
15%	120.13±6.87/0.053	−24.65±9.36	12.16±0.01	98.4±0.1
20%	135.47±8.46/0.057	−27.31±3.32	16.91±0.06	89.4±0.3
30%	162.4±11.69/0.061	−35.56±2.65	20.67±0.03	88.3±0.1

PI means polydispersity index, *DL* drug loading content, *EE* encapsulation efficiency
[a] Mean diameter in purified water was measured by DLS

increased accumulation in tumors, and better control of drug release (36,37). In addition, we speculated that certain components in the serum, such as opsonin, could bind to the surface of nanoparticles, thereby slightly increasing the particle size in bovine serum at the beginning of investigation (38).

X-ray Powder Diffraction and Circular Dichroism Spectrum

The physical state of the PTX formulated in NPs-PTX was compared with PTX crystal and Abraxane® using XRD. As shown in Fig. 3, PTX powder displayed a few typical diffraction peaks at 5.6°, 9.9°, and 12.7° (a), suggesting that it was crystalline (39). Meanwhile, the physical mixture of PTX and HSA retained the characteristic peaks of PTX, indicating that PTX in the mixture was also crystalline (c). However, typical diffraction peaks of PTX disappeared in NPs-PTX (d) and Abraxane® (e) and their diffraction patterns were the same as that of HSA (b), suggesting that the PTX dispersed in both NPs-PTX and Abraxane® were in a noncrystalline, amorphous state (18,30,40). This was a readily bioavailable state which allowed fast drug release from nanoparticles following i.v. administration (18,30). More importantly, this result suggested that we had prepared nanoparticles where PTX could be as bioavailable as in Abraxane®.

CD was utilized to examine the change in HSA secondary structures in NPs-PTX and Abraxane®. From Fig. 4a, it was revealed that there was scarcely any difference in far ultraviolet range from 190 to 250 nm for NPs-PTX compared with natural HSA. Furthermore, calculating the data on the basis of the method of Yang *et al.* (28,29), we obtained the proportions of various secondary structures, including α helix, β sheet, and random coil of HSA. The result showed that there was also nearly no variance between NPs-PTX and native HSA (Fig. 4b).

***In Vitro* Cytotoxicity**

To evaluate whether NPs-PTX could enhance the cytotoxicity of PTX, *in vitro* experiments of PTX, NPs-PTX, against MCF-7 and A549 cell lines were performed. In MCF-7 cells, a dose-dependent cytotoxicity was observed, as shown in Fig. 5a. With the increase of PTX concentration, NPs-PTX and Abraxane® began to display cytotoxicity at 27 ng/mL, while this concentration for PTX was 2.7 ng/mL. Ranging from 27 to 270 ng/mL, NPs-PTX and Abraxane® displayed relatively the same cell inhibition as PTX, indicating an equivalent cytotoxicity. This was demonstrated by the calculated IC_{50} values between all formulations, where NPs-PTX even showed a lower IC_{50} value (27.7 ng/mL) than PTX (74.1 ng/mL) and Abraxane® (65.4 ng/mL) (Fig. 5b). Similarly, a dose-dependent

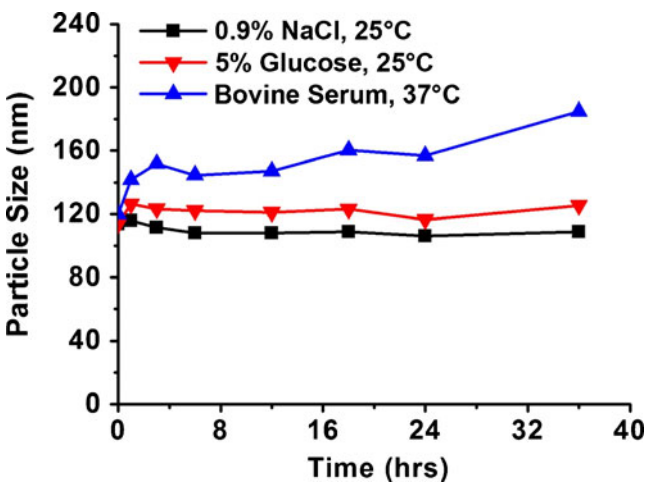

Fig. 2. Stability of NPs-PTX in different conditions. NPs-PTX (5 mg/mL) were reconstituted in 0.9% NaCl, 5% glucose, and bovine serum, respectively

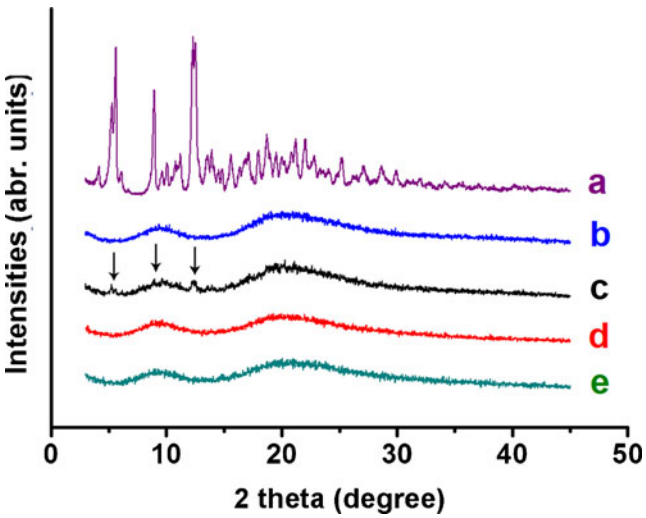

Fig. 3. XRD patterns of NPs-PTX. *a* PTX; *b* HSA; *c* physical mixture of PTX and HSA (1:9, w/w), the *arrows* point out typical diffraction peaks of PTX in the mixture; *d* NPs-PTX (1:9 PTX/HSA, w/w); *e* Abraxane®

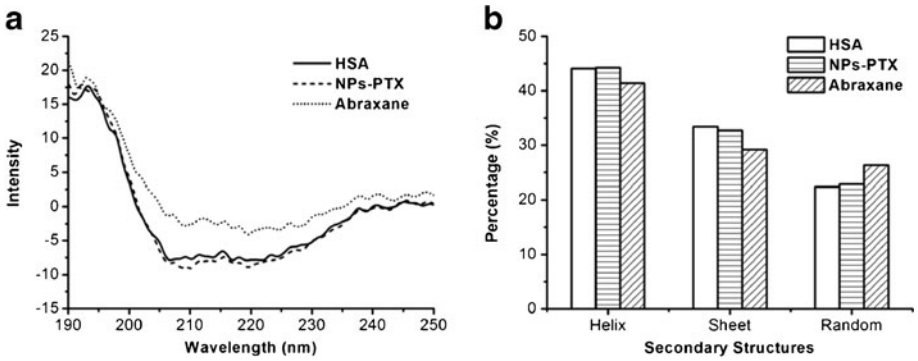

Fig. 4. Secondary structure of NPs-PTX. **a** CD spectrum of HSA, NPs-PTX, and Abraxane®; **b** percentages of various secondary structures of HSA, NPs-PTX, and Abraxane®

cytotoxicity of NPs-PTX, Abraxane®, and PTX against A549 cells was also observed from Fig. 5c. Calculation also revealed a much lower IC_{50} value of NPs-PTX (31.0 ng/mL) and Abraxane® (19.2 ng/mL) than PTX (191.9 ng/mL), and both differences were statistically significant ($P<0.05$) (Fig. 5d). The cytotoxicity difference among various cell lines may be attributed to the differences in their genetic background and biological behavior (30). Based on these results, we speculated that NPs-PTX could increase the pharmacological effectiveness of PTX to different extents against various tumor cells, and this improvement was as high as Abraxane®.

In Vitro Cellular Uptake of NPs-PTX

The cellular uptake study of NPs-PTX was conducted on MCF-7 cells. First, the intracellular distribution of NPs-PTX-Cou-6 in MCF-7 cells was examined by CLSM. As shown in Fig. 6a, d, the green fluorescence (Cou-6) was closely around the nuclei (blue, stained by DAPI), suggesting that NPs-PTX-Cou-6 were internalized by MCF-7 cells and distributed in the cytoplasm. In addition, we obtained a series of merged pictures from top to bottom at the *z*-axis direction of the cells (Supplementary Fig. 2), which further demonstrated this point of view.

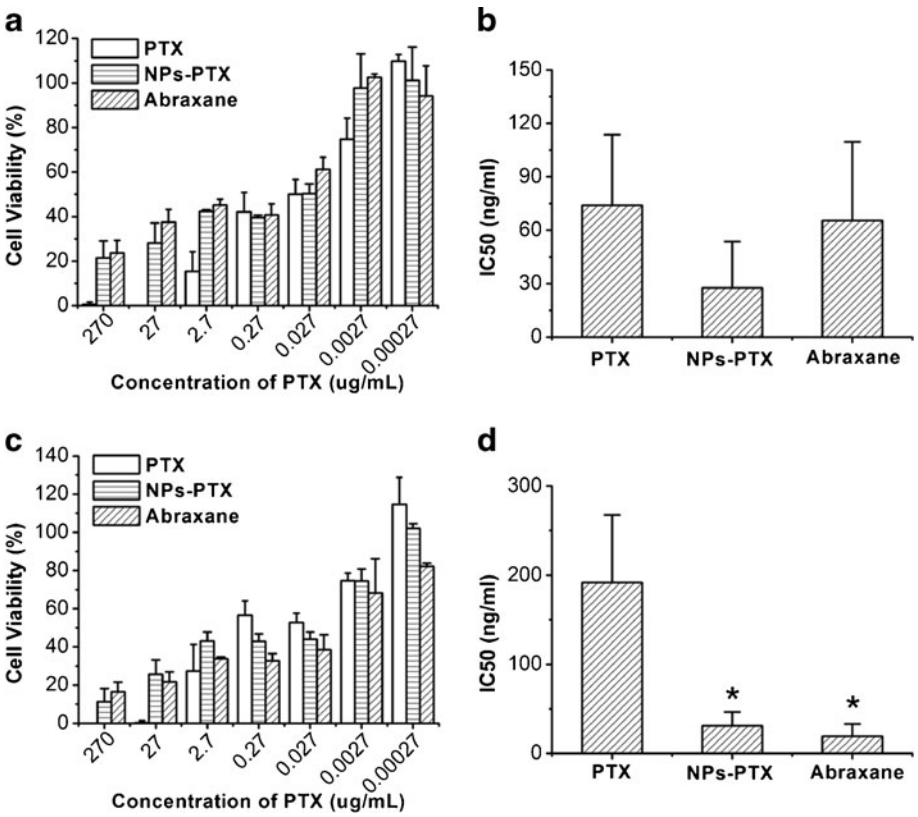

Fig. 5. *In vitro* cytotoxicity of NPs-PTX. **a** Cell viability of MCF-7 against PTX, NPs-PTX, and Abraxane® for 48 h co-incubation; **b** calculated IC_{50} values of PTX, NPs-PTX, and Abraxane® against MCF-7 cells; **c** cell viability of A549 against PTX, NPs-PTX, and Abraxane® for 48 h co-incubation; **d** calculated IC_{50} of PTX, NPs-PTX, and Abraxane® against A549 cells. The results represent the mean±SD ($n=3$–4). *$P<0.05$ compared with PTX

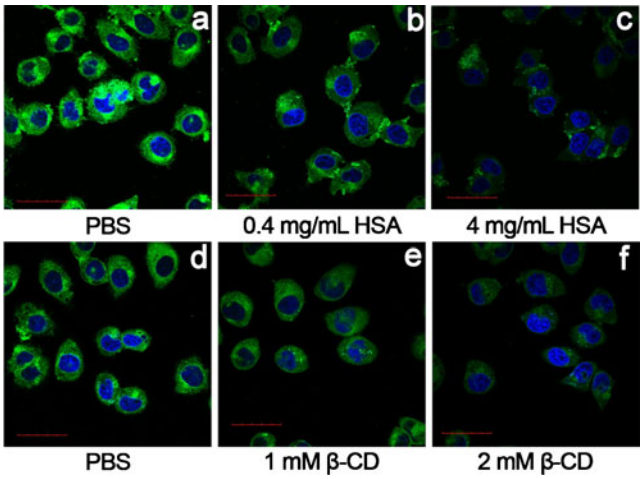

Fig. 6. Confocal image of NPs-PTX-Cou-6 distribution in MCF-7 cells. Cells were preincubated with **a** PBS, **b** 0.4 mg/mL HSA, **c** 4 mg/mL HSA, **d** PBS, **e** 1 mM β-CD, and **f** 2 mM β-CD, respectively, before they were subjected to NPs-PTX-Cou-6. All scale bars stand for 50 μm

In the following, HSA and β-CD were utilized to block MCF-7 cellular uptake of NPs-PTX-Cou-6. When co-incubated with 0.4 mg/mL HSA (Fig. 6b), less NPs-PTX-Cou-6 (green) was internalized into MCF-7 cells compared with PBS (Fig. 6a), revealing that MCF-7 cell uptake was inhibited by free HSA. We also observed a dose-dependent inhibition on the uptake of NPs-PTX-Cou-6 (Fig. 6a–c) when the concentration of HSA increased from 0.4 to 4 mg/mL. Moreover, it was revealed that the uptake of NPs-PTX-Cou-6 could also be dose-dependently suppressed by β-CD from 0 mM (PBS) to 2 mM (Fig. 6d–f).

Afterwards, to further confirm the inhibition effects of HSA and β-CD on MCF-7 cellular uptake of NPs-PTX, we conducted the FCM examination. It was seen that 0.4 and 4 mg/mL HSA could shift the cells' fluorescence–count curve to the left in a dose-dependent manner (Fig. 7a). By calculating the mean fluorescence intensity of 10,000 cells in each sample, we found that it decreased 39% and 69% by 0.4 and 4 mg/mL HSA, respectively. Finally, 1 and 2 mM β-CD could also shift the cells' fluorescence–count curve to the left in a dose-related style (Fig. 7b) and the mean fluorescence intensity of 10,000 cells decreased 40% and 57% by 1 and 2 mM β-CD, respectively.

The combination of results from CLSM and FCM examinations on cellular uptake strongly indicated that NPs-PTX was internalized into tumor cells through the specific interaction between HSA of nanoparticles and HSA receptors, such as SPARC receptors (18,19). SPARC is a secreted glycoprotein highly expressed on cell surfaces of various tumors, including breast, prostate, liver, lung, kidney, gastric, colorectal, skin melanoma, *etc*., which could be blocked by free HSA (41). Moreover, according to the fact that β-CD was an inhibitor of "caveolar" and β-CD's inhibition on cellular uptake demonstrated in the CLSM and FCM examinations, we speculated that NPs-PTX might also be internalized into tumor cells via "caveolars" after binding with HSA receptors on cell surfaces. Both the HSA–SPARC interaction and "caveolars" mediated the internalization of NPs-PTX into tumor cells.

Real-Time Biodistribution of NPs-PTX

To monitor the real-time distribution, excretion, and tumor-targeting efficiency of NPs-PTX *in vivo*, noninvasive near infrared fluorescence optical imaging technology was employed in this study. Mice bearing the H22 tumor were selected as the animal model and a near infrared fluorescence dye, NIR-775, was employed as the imaging agent. Near infrared dyes could enable deep tissue imaging with high penetration but low tissue absorption and scattering (42). To simulate the same physicochemical characteristics of nanoparticles, only 10% of NIR-775 (NIR-775/PTX, *w*/*w*) was co-packaged into NPs-PTX. Equivalent dosages of free NIR-775 and NPs-PTX-NIR-775 were injected into H22 tumor-bearing mice, after which near infrared fluorescence signals were clearly and quickly observed, as shown by Fig. 8. In the first 3 h, a high level of fluorescence intensity was detected in the liver when mouse were injected with NPs-PTX-NIR-775, which was similar to free NIR-775. However, this high fluorescence intensity quickly disappeared in the following hours due to metabolism (12,30). On the other aspect, an accumulation of NPs-PTX-NIR-775 was observed

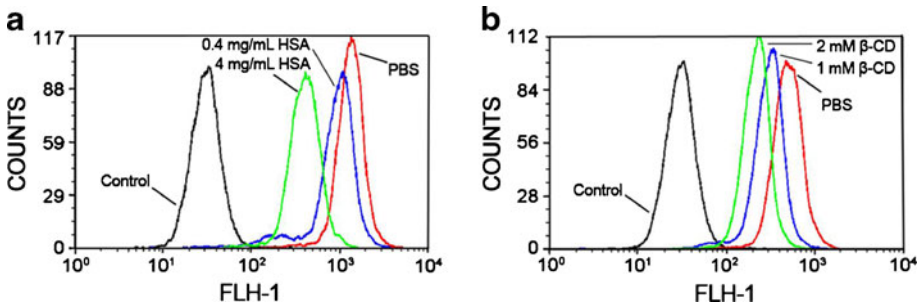

Fig. 7. Quantification of cell uptake for NPs-PTX-Cou-6 by FCM. NPs-PTX-Cou-6 and different concentrations of free **a** HSA and **b** β-CD were co-incubated with MCF-7 cells. The mean fluorescence intensities of 10,000 cells were determined. All results revealed the fluorescence of cells at 527 nm and the exciting wavelength was set at 490 nm (*FLH-1*)

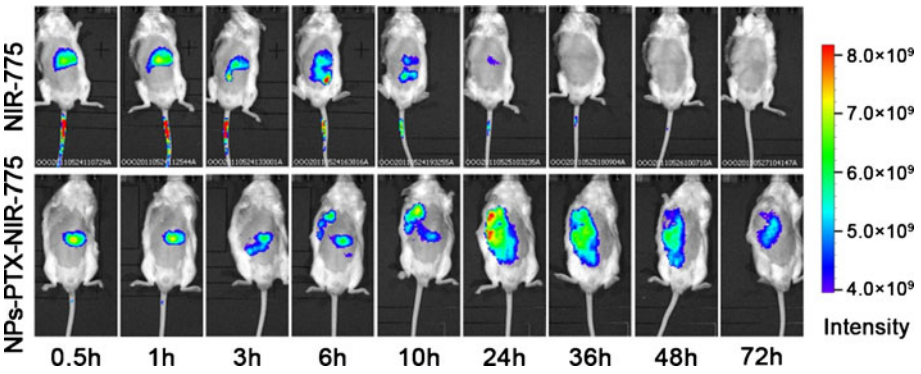

Fig. 8. The NIRF images of H22 tumor-bearing mice following i.v. injection of free NIR-775 and NPs-PTX-NIR-775

in the tumor area after 3 h post injection. Near infrared fluorescence intensity in tumor was gradually enhanced compared to normal tissues after injection, reached its peak at 24 h, and remained at a relatively high level up to 72 h. Nonetheless, there was no obvious increase of fluorescence intensity in tumors of the mouse treated with free NIR-775 up to 72 h post injection. This tumor accumulation directly proved the *in vivo* targeting ability of NPs-PTX and it might result from the EPR effects (3,11). We speculated that the HSA–SPARC interaction was also responsible for facilitating the accumulation of NPs-PTX in tumors *in vivo* as it has been recently determined that SPARC binding to albumin was saturable and specific and might play an important role in the increased tumor accumulation of albumin-bound drugs (19).

In Vivo Antitumor Efficacy

To evaluate the *in vivo* antitumor efficiency of NPs-PTX on H22 tumor-bearing mice, saline, PTX (13.4 mg/kg), Abraxane® (30 mg PTX/kg), and NPs-PTX (30 mg PTX/kg) were intravenously injected into animals on days 1 and 3, respectively. As shown in Fig. 9a, in the saline group, tumors quickly and continuously grew after injection and the average tumor volume on day 19 was up to 12.69 cm^3 (about 0.1 cm^3 on day 1). In all other three groups, the curves overlapped with each other and tumor volumes were increased slower than the saline group before day 10. After day 10, tumors in the three groups grew much more slower than the saline group and their volumes were more and more apart from each other, with PTX group the largest (8.15 cm^3), Abraxane® in the middle (6.52 cm^3), and NPs-PTX group the smallest (4.98 cm^3) on day 19. Comparing the mean tumor volumes of saline, the inhibition rate of PTX, Abraxane®, and NPs-PTX was 35.8%, 48.6%, and 60.8%, respectively. In addition, the survival curves of tumor-bearing mice in each group are shown in Fig. 9b. All mice treated with saline died within 34 days, while three of five mice in both PTX and Abraxane® groups died on day 31. Only one of four mice in the NPs-PTX group died at the end of measurement.

Based on the smallest mean tumor volume, slowest tumor growth rate, and longest animal survival time, it was clear that NPs-PTX showed an enhanced *in vivo* antitumor effect for PTX. The noticeable enhanced antitumor effect of NPs-PTX *in vivo* should be attributed to the following factors: (1) The existence of negative charges on the nanoparticles' surfaces (Table I) guaranteed a good stability for nanoparticles, making them easier to accumulate in tumors due to the EPR effect. (2) More importantly, as demonstrated in real-time imaging, NPs-PTX displayed a prominent and relatively lasting tumor targeting, thus leading to high PTX accumulation and improvement of therapeutic index of PTX.

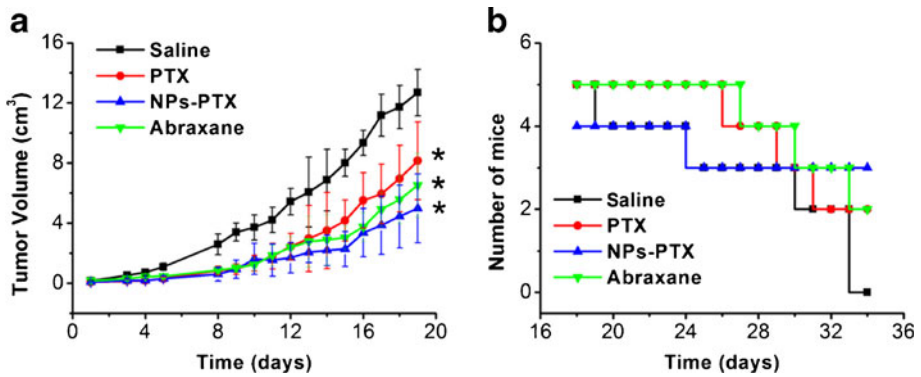

Fig. 9. Antitumor efficiency of NPs-PTX in H22 tumor-bearing mice. **a** Tumor volumes after injection of saline, PTX, NPs-PTX, and Abraxane®. **b** Survival of tumor-bearing mice in various groups. *$P<0.05$ compared with saline

CONCLUSION

In summary, novel self-assembling HSA nanoparticles for targeted delivery of PTX to tumors were successfully developed in this study. This simple strategy pioneered the idea of fabricating drug-loaded nanoparticles with protein unfolding and self-assembly. It eliminated the complicated preparations and toxicities of residual organic solvents and cross-linking agents in other formulations. The physicochemical features, *in vitro* cytotoxicity and cellular uptake, real-time biodistribution, and antitumor efficacy were evaluated. These studies revealed NPs-PTX's readily bioavailable state of PTX, highly retained HSA secondary structures, HSA receptor-mediated cellular internalization, enhanced cytotoxicity, lasting *in vivo* tumor targeting, and better antitumor effectiveness. This study not only offers a novel and more efficient strategy for PTX in tumor chemotherapy but also paves the way for many other hydrophobic drugs by improving their clinical effectiveness for cancer therapy.

ACKNOWLEDGMENTS

This paper was supported by the Research Fund for the Doctoral Program of Higher Education of China (no. 20110091120044), the Natural Science Foundation of Jiangsu (nos. BK2011572 and BK2011539), the National Natural Science Foundation (nos. 81202474 and 30973651), the Changzhou Special Project of Biotechnology and Biopharmacy (no. CE20105006), the Science and Technology Support Program of Jiangsu Province (no. BE2010719), and the Postdoctoral Foundation (no. 2012M521051).

REFERENCES

1. Peer D, Karp JM, Hong S, Farokhzad OC, Margalit R, Langer R. Nanocarriers as an emerging platform for cancer therapy. Nat Nanotechnol. 2007 Dec;2(12):751–60.
2. MacKay JA, Chen M, McDaniel JR, Liu W, Simnick AJ, Chilkoti A. Self-assembling chimeric polypeptide–doxorubicin conjugate nanoparticles that abolish tumours after a single injection. Nat Mater. 2009 Dec;8(12):993–9.
3. Cho K, Wang X, Nie S, Chen ZG, Shin DM. Therapeutic nanoparticles for drug delivery in cancer. Clin Cancer Res. 2008 Mar 1;14(5):1310–6.
4. Duncan R. Polymer conjugates as anticancer nanomedicines. Nat Rev Cancer. 2006 Sep;6(9):688–701.
5. Greish K. Enhanced permeability and retention of macromolecular drugs in solid tumors: a royal gate for targeted anticancer nanomedicines. J Drug Target. 2007 Aug–Sep;15(7–8):457–64. PubMed PMID: 17671892.
6. Lee CC, MacKay JA, Frechet JM, Szoka FC. Designing dendrimers for biological applications. Nat Biotechnol. 2005 Dec;23(12):1517–26.
7. Gratton SE, Pohlhaus PD, Lee J, Guo J, Cho MJ, Desimone JM. Nanofabricated particles for engineered drug therapies: a preliminary biodistribution study of PRINT nanoparticles. J Control Release. 2007 Aug 16;121(1–2):10–8.
8. Pan J, Chan SY, Lee WG, Kang L. Microfabricated particulate drug-delivery systems. Biotechnol J. 2011 Dec;6(12):1477–87.
9. Duncan R. The dawning era of polymer therapeutics. Nat Rev Drug Discov. 2003 May;2(5):347–60.
10. Ferrari M. Cancer nanotechnology: opportunities and challenges. Nat Rev Cancer. 2005 Mar;5(3):161–71.
11. Davis ME, Chen ZG, Shin DM. Nanoparticle therapeutics: an emerging treatment modality for cancer. Nat Rev Drug Discov. 2008 Sep;7(9):771–82.
12. Xiao K, Luo J, Fowler WL, Li Y, Lee JS, Xing L, *et al.* A self-assembling nanoparticle for paclitaxel delivery in ovarian cancer. Biomaterials. 2009 Oct;30(30):6006–16.
13. Rihova B. Biocompatibility of biomaterials: hemocompatibility, immunocompatiblity and biocompatibility of solid polymeric materials and soluble targetable polymeric carriers. Adv Drug Deliv Rev. 1996;21(2):157–76.
14. Maham A, Tang Z, Wu H, Wang J, Lin Y. Protein-based nanomedicine platforms for drug delivery. Small. 2009 Aug 3;5(15):1706–21.
15. Fung SY, Yang H, Bhola PT, Sadatmousavi P, Muzar E, Liu M, *et al*. Self-assembling peptide as a potential carrier for hydrophobic anticancer drug ellipticine: complexation, release and in vitro delivery. Adv Funct Mater. 2009;19(1):74–83.
16. Elzoghby AO, Samy WM, Elgindy NA. Albumin-based nanoparticles as potential controlled release drug delivery systems. J Control Release. 2012 Jan 30;157(2):168–82.
17. McDaniel JR, Callahan DJ, Chilkoti A. Drug delivery to solid tumors by elastin-like polypeptides. Adv Drug Deliv Rev. 2010 Dec 30;62(15):1456–67.
18. Desai N. Nab technology: a drug delivery platform utilizing endothelial gp60 receptor-based transport and tumour-derived SPARC for targeting. Drug Delivery Report 16th edition; 2007. p. 37–41.
19. Desai N, Trieu V, Yao Z, Louie L, Ci S, Yang A, *et al*. Increased antitumor activity, intratumor paclitaxel concentrations, and endothelial cell transport of cremophor-free, albumin-bound paclitaxel, ABI-007, compared with cremophor-based paclitaxel. Clin Cancer Res. 2006 Feb 15;12(4):1317–24.
20. Damascelli B, Cantu G, Mattavelli F, Tamplenizza P, Bidoli P, Leo E, *et al*. Intraarterial chemotherapy with polyoxyethylated castor oil free paclitaxel, incorporated in albumin nanoparticles (ABI-007): phase II study of patients with squamous cell carcinoma of the head and neck and anal canal: preliminary evidence of clinical activity. Cancer. 2001 Nov 15;92(10):2592–602.
21. Bale AS, Barone Jr S, Scott CS, Cooper GS. A review of potential neurotoxic mechanisms among three chlorinated organic solvents. Toxicol Appl Pharmacol. 2011 Aug 15;255(1):113–26.
22. Xu R, Fisher M, Juliano RL. Targeted albumin-based nanoparticles for delivery of amphipathic drugs. Bioconjug Chem. 2011 May 18;22(5):870–8.
23. Gong J, Huo M, Zhou J, Zhang Y, Peng X, Yu D, *et al*. Synthesis, characterization, drug-loading capacity and safety of novel octyl modified serum albumin micelles. Int J Pharm. 2009 Jul 6;376(1–2):161–8.
24. Zhao Q, Chen W, Chen Y, Zhang L, Zhang J, Zhang Z. Self-assembled virus-like particles from rotavirus structural protein VP6 for targeted drug delivery. Bioconjug Chem. 2011 Mar 16;22(3):346–52.
25. Dreher MR, Simnick AJ, Fischer K, Smith RJ, Patel A, Schmidt M, *et al*. Temperature triggered self-assembly of polypeptides into multivalent spherical micelles. J Am Chem Soc. 2008 Jan 16;130(2):687–94.
26. Pinto Reis C, Neufeld RJ, Ribeiro AJ, Veiga F. Nanoencapsulation methods for preparation of drug-loaded polymeric nanoparticles. Nanomedicine. 2006 Mar;2(1):8–21.
27. Hu Y, Wu J, Ding D, Gong G, Tang X, Tong C, *et al*., inventors; WO Patent WO/2011/017,835, assignee. Preparation method of protein or peptide nanoparticles for in vivo drug delivery by unfolding and refolding. 2011.
28. Yang JT, Wu CS, Martinez HM. Calculation of protein conformation from circular dichroism. Methods Enzymol. 1986;130:208–69.
29. Villoutreix BO, Garcia de Frutos P, Lovenklev M, Linse S, Fernlund P, Dahlback B. SHBG region of the anticoagulant cofactor protein S: secondary structure prediction, circular dichroism spectroscopy, and analysis of naturally occurring mutations. Proteins. 1997 Dec;29(4):478–91. PubMed PMID: 9408945.
30. Zhu Z, Li Y, Li X, Li R, Jia Z, Liu B, *et al*. Paclitaxel-loaded poly(*N*-vinylpyrrolidone)-*b*-poly(epsilon-caprolactone) nanoparticles:

preparation and antitumor activity in vivo. J Control Release. 2010 Mar 19;142(3):438–46.
31. Yu DH, Lu Q, Xie J, Fang C, Chen HZ. Peptide-conjugated biodegradable nanoparticles as a carrier to target paclitaxel to tumor neovasculature. Biomaterials. 2010 Mar;31(8): 2278–92.
32. Davda J, Labhasetwar V. Characterization of nanoparticle uptake by endothelial cells. Int J Pharm. 2002 Feb 21;233(1–2):51–9.
33. Frei E. Albumin binding ligands and albumin conjugate uptake by cancer cells. Diabetol Metab Syndr. 2011;3(1):11.
34. He XM, Carter DC. Atomic structure and chemistry of human serum albumin. Nature. 1992 Jul 16;358(6383):209–15.
35. Galantini L, Leggio C, Konarev PV, Pavel NV. Human serum albumin binding ibuprofen: a 3D description of the unfolding pathway in urea. Biophys Chem. 2010 Apr;147(3):111–22.
36. Wang J, Sui M, Fan W. Nanoparticles for tumor targeted therapies and their pharmacokinetics. Curr Drug Metab. 2010 Feb;11(2):129–41.
37. Venkatraman SS, Ma LL, Natarajan JV, Chattopadhyay S. Polymer- and liposome-based nanoparticles in targeted drug delivery. Front Biosci (Schol Ed). 2010;2:801–14.
38. Singh R, Lillard Jr JW. Nanoparticle-based targeted drug delivery. Exp Mol Pathol. 2009 Jun;86(3):215–23.
39. Liu X, Lei L, Hou JW, Tang MF, Guo SR, Wang ZM, *et al*. Evaluation of two polymeric blends (EVA/PLA and EVA/PEG) as coating film materials for paclitaxel-eluting stent application. J Mater Sci: Mater Med. 2011 Feb;22(2):327–37.
40. Lu Z, Yeh TK, Tsai M, Au JL, Wientjes MG. Paclitaxel-loaded gelatin nanoparticles for intravesical bladder cancer therapy. Clin Cancer Res. 2004 Nov 15;10(22):7677–84.
41. Framson PE, Sage EH. SPARC and tumor growth: where the seed meets the soil? J Cell Biochem. 2004 Jul 1;92(4):679–90.
42. Peng L, Liu R, Marik J, Wang X, Takada Y, Lam KS. Combinatorial chemistry identifies high-affinity peptidomimetics against alpha4beta1 integrin for in vivo tumor imaging. Nat Chem Biol. 2006 Jul;2(7):381–9.